Comparative Analysis and Optimization of Novel Pulse Injection Sensorless Drive Methods for Fault-Tolerant DC Vernier Reluctance Machine

Weiyu Wang, *Graduate Student Member, IEEE*, Xing Zhao, *Member, IEEE*, Shuangxia Niu, *Senior Member, IEEE*, and Weinong Fu

***Abstract*—Multiphase dc-excited Vernier reluctance machine (DC-VRM) exhibits the merits of robust structure, small torque ripple, and good fault-tolerant ability. Developing advanced sensorless drive methods can further promote its application in the safety-critical system. In this article, pulse injection sensorless drive methods are optimized in a six-phase DC-VRM parallel H-bridge drive system to strengthen their acceleration performance and fault-tolerant ability. The acceleration performance studied in this article corresponds to the acceleration speed during the startup stage. By the full-phase alternative pulse injection method (APIM), each phase can be excited independently to avoid mutual-inductance influence on position estimation, but this method suffers from a long communication delay and relatively poor acceleration performance. A reduced-phase APIM can reduce detection time, but the lack of detected phase may influence position estimation accuracy and fault-tolerant ability. To solve these problems, a novel vertical-axis synchronous pulse injection method is proposed and compared with previous methods in this article. The key is to inject detection pulses into vertical-axis phases simultaneously, thus reducing the detection time and improving the torque generation. It is proved that the influence of mutual inductance on position estimation can be ignored, and the detection accuracy and acceleration performance can be improved without deterioration of fault-tolerant ability.**

***Index Terms*—DC-excited vernier reluctance machine (DC-VRM), sensorless drive, vertical-axis synchronous pulse injection.**

I. Introduction

With an increasing emphasis on environmental protection and energy saving, the research on transportation electrification shows an upward trend [1], [2]. Nonpermanent magnets doubly salient reluctance machines with robust structure and harsh environment adaption have attracted a lot of attention [3], [4]. Switched reluctance machine (SRM) suffers from large torque ripple and noises because of half-cycle conduction [5]. Doubly fed doubly salient machine (DF-DSM) can be operated in the whole electrical period, but the torque ripple is still unsatisfied due to the unbalanced magnetic distribution and rich even-order flux harmonics [6]. Illustrated by the emerging flux modulation theory [7], [8], a new type of dc-excited Vernier reluctance machine (DC-VRM) exhibits the merits of small torque ripple and minimum cogging torque [9], [10].

Multiphase fault-tolerant machine with the parallel drive is widely applied to aerospace applications and electrical propulsion systems [11], [12]. By eliminating vulnerable position sensors, system reliability can be further improved by sensorless drive. The high-speed sensorless drive has been relatively mature [13]–[16], while the detected signal has a low signal-to-noise ratio at zero or low-speed range. For doubly salient reluctance machine low-speed sensorless drive, modulation method [17], [18], sense coil method [19], [20], current waveform method [21], [22], and pulse injection method [23]–[30] are typical strategies. In the modulation method, by injecting a high-frequency detection signal into the idle phase through an oscillator, the modulated signal is detected by the demodulation circuit, and a switching circuit is required [17], [18]. In the sense coil method [19], [20], the parallel sense coils are embedded in the slots in reverse series to minimize the mutual-inductance coupling. Full-cycle position detection without a switch circuit can be achieved, but this method also requires additional excitation sources and detection circuits.

Without additional hardware, the current waveform method detects the current slop in the current chopping control process and combines the incremental inductance model to estimate rotor position [21], [22]. However, with the increase in speed, the number of current chopping waves decreases, so the position detection accuracy is hard to be guaranteed. In addition, the saturation effect of the magnetic circuit needs to be considered, and the machine parameters measurement or fitting is necessary [22]. The pulse injection method does not require *prior* knowledge of the machine parameters, but only applies narrow detection pulses injected into the idle phase to detect the inductance indirectly. As the resultant current amplitudes are small, the saturation effect can be ignored to simplify the calculation.

Manuscript received 9 August 2021; revised 3 December 2021, 22 February 2022, and 20 April 2022; accepted 7 June 2022. Date of publication 13 June 2022; date of current version 26 July 2022. This work was supported in part by the National Natural Science Foundation of China under Project 52077187 and in part by the Research Grant Council of the Hong Kong Government under Projects PolyU 152143/18E and PolyU 152109/20E. Recommended for publication by Associate Editor J. B. He. *(Corresponding author: Shuangxia Niu.)*

Weiyu Wang and Shuangxia Niu are with the Department of Electrical Engineering, The Hong Kong Polytechnic University, Hong Kong (e-mail: weiyu.wang@connect.polyu.hk; eesxniu@polyu.edu.hk).

Xing Zhao is with the Department of Electronic Engineering, University of York, YO10 5DD York, U.K. (e-mail: xing.zhao@york.ac.uk).

Weinong Fu is with the Shenzhen Institutes of Advanced Technology, Chinese Academy of Sciences, Shenzhen 518100, China (e-mail: wn.fu@siat.ac.cn).

Color versions of one or more figures in this article are available at https://doi.org/10.1109/TPEL.2022.3182054.

Digital Object Identifier 10.1109/TPEL.2022.3182054

Combining the methods of the inductance Fourier model [23], inductance linearity characteristics [24], inductance threshold comparison [25], or inductance vectors [26], the conduction phase can be decided.

However, due to the half-cycle conduction principle of SRM, detection pulses are injected into the idle phase, thereby the negative torque is produced, and the full-cycle inductance detection cannot be realized. For DF-DSM, the detection pulses are injected in the time interval between consecutive acceleration pulses [27], thereby full-cycle inductance detection can be acquired. While the communication delay is inevitable because of the discrete detection. To ease this issue, reducing detection time is a potential strategy [28]–[30]. According to the present conduction state, a single detection pulse is injected, and its resultant current amplitude is compared with that of the acceleration current consuming the same time to determine whether the rotor has reached the next sector [28]. Similarly, a method based on the three-phase pulse injection is proposed in which the conduction phase is determined by comparing the resultant current amplitudes of parallel phases [29]. Unfortunately, these methods highly depend on the present conduction state and lack fault-tolerant ability. In [30], a two-step three-phase pulse injection method is proposed to balance the performance.

Mutual inductances between armature windings are not considered in the above DF-DSM sensorless drive methods but cannot be overlooked in DC-VRM sensorless drives. In this article, optimized sensorless drive methods are performed in a six-phase DC-VRM with a parallel H-bridge-converter drive to achieve a solution that combines sensorless merits, low torque ripple, and high tracking performance. Also, the fault-tolerant ability is provided not only for open-circuit fault but also for current sampling fault. First, by the full-phase alternative pulse injection method (full-phase APIM), mutual-inductance influence on position estimation can be avoided. Then, the inherent communication delay is decreased by the reduced-phase alternative pulse injection method (reduced-phase APIM), but the detection accuracy and reliability are traded off. To solve these problems, a novel vertical-axis synchronous pulse injection method (vertical-axis SPIM) is proposed. The key is to inject detection pulses into the stator-side vertical-axis phases simultaneously to shorten detection time and avoid the inductance detection bias fundamentally. Moreover, the mutual inductance between the vertical-axis phases is slight and shows an evitable influence on position estimation. A solution that combines accurate position detection, high acceleration performance, and strong fault-tolerant ability can be achieved.

The rest of this article is organized as follows. In Section II, the six-phase DC-VRM mathematical model and the inductance characteristics are introduced. In Section III, full-phase APIM as well as indicators influence acceleration performance are illustrated. In Section IV, reduced-phase APIMs are discussed. In Section V, the proposed vertical-axis SPIM is analyzed. In Section VI, a fault diagnosis for fault-tolerant operation is proposed. In Section VII, a test bench is built, and the experimental results are shown. The discussion is presented in Section VIII. Finally, Section IX concludes this article.

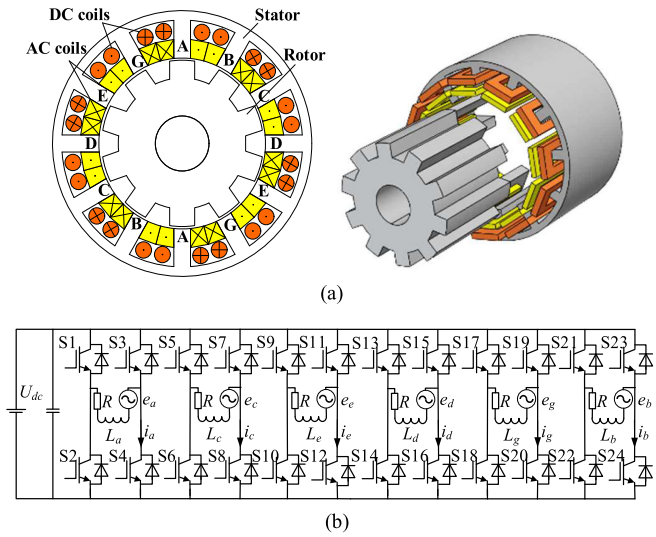

Fig. 1. (a) Structure of six-phase DC-VRM. (b) Parallel H-bridge converter.

II. Configuration of Six-Phase DC-VRM

A. H-Bridge-Converter-Based Sensorless Drive System

The structure of the six-phase DC-VRM to be studied is provided in Fig. 1(a). The dc field coils are wounded on each stator tooth, and the directions of two adjacent dc field coils are opposite. All the dc field coils are connected in series to form one single dc field winding. Six ac armature coils are wounded on each stator tooth as well. A pair of vertical-axis phases are defined as two phases in which the wound stator teeth are vertical in space. For example, phase A and phase D are a pair of vertical-axis phases.

The parallel H-bridge drive configuration is shown in Fig. 1(b). The advantages of the parallel H-bridge-converter-based sensorless DC-VRM drive system can be summarized as follows.

1) Using a parallel H-bridge converter allows each phase to be independently excited; thus, the detection pulses can be flexibly regulated to improve acceleration performance.
2) The H-bridge drive structure shows a significant advantage in fault tolerant to improve system reliability.
3) This drive system keeps the complementary electromagnetic characteristic of six-phase DC-VRM in reducing torque ripple.

B. Mathematical Model

The current and inductance equations can be expressed as

$$I = [i_a \quad i_b \quad i_c \quad i_d \quad i_e \quad i_g \quad i_f]^T \tag{1}$$

$$L = \begin{bmatrix} L_a & L_{ab} & L_{ac} & L_{ad} & L_{ae} & L_{ag} & L_{af} \\ L_{ab} & L_b & L_{bc} & L_{bd} & L_{be} & L_{bg} & L_{bf} \\ L_{ac} & L_{bc} & L_c & L_{cd} & L_{ce} & L_{cg} & L_{cf} \\ L_{ad} & L_{bd} & L_{cd} & L_d & L_{de} & L_{dg} & L_{df} \\ L_{ae} & L_{be} & L_{ce} & L_{de} & L_e & L_{eg} & L_{ef} \\ L_{ag} & L_{bg} & L_{cg} & L_{dg} & L_{eg} & L_g & L_{gf} \\ L_{af} & L_{bf} & L_{cf} & L_{df} & L_{ef} & L_{gf} & L_f \end{bmatrix} \tag{2}$$

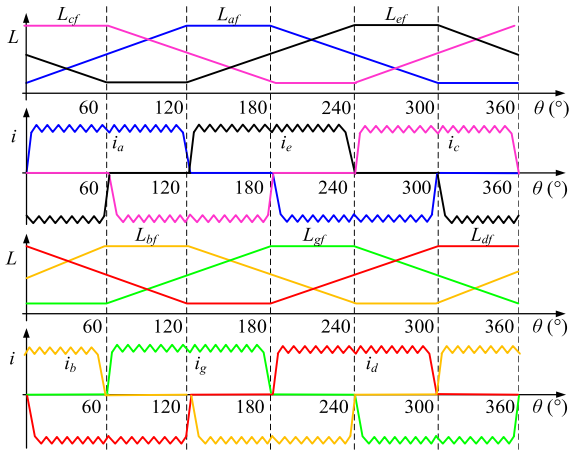

Fig. 2. Conduction mode of six-phase DC-VRM.

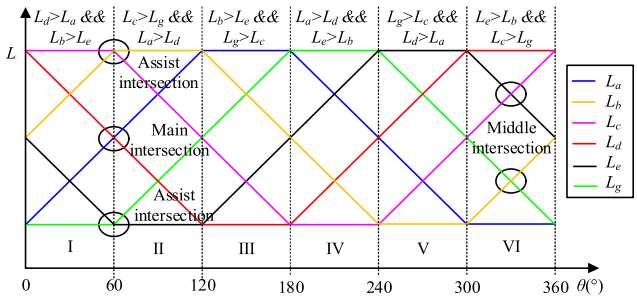

Fig. 3. Self-inductances and inductance intersections.

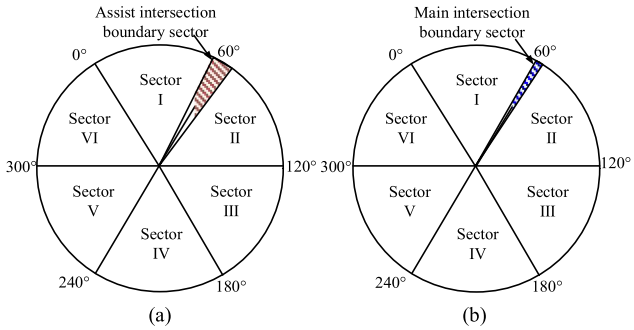

Fig. 4. Boundary sector division. (a) Assist intersection. (b) Main intersection.

where I is the current matrix, i_a, i_b, i_c, i_d, i_e, and i_g are the phase currents, i_f is the field current, L is the inductance matrix, L_{af}, L_{bf}, L_{cf}, L_{df}, L_{ef}, and L_{gf} are the mutual inductances between armature windings and the field winding, L_a, L_b, L_c, L_d, L_e, and L_g are the phase self-inductances, L_{ab}, L_{ac}, L_{ad}, L_{ae}, L_{ag}, L_{bc}, L_{bd}, L_{be}, L_{bg}, L_{cd}, L_{ce}, L_{cg}, L_{de}, L_{dg}, and L_{eg} are the mutual inductances between armature windings, and L_f is the self-inductance of the field winding. Taking phase A as an example, the torque components under current excitation can be expanded as

$$T_a = i_a\, i_f \frac{dL_{af}}{d\theta} + \frac{1}{2} i_a^2 \frac{dL_a}{d\theta} + \frac{1}{2} i_f^2 \frac{dL_f}{d\theta} \tag{3}$$

where T_a is the total torque, and θ is the electrical angle. The first term of (3) is the major component of the excitation torque produced by the mutual inductance between the dc field winding and the ac winding. The second term is the reluctance torque produced by the variation of self-inductance. As bipolar current excitation, the average reluctance torque in the whole electrical period is zero. The third term is the cogging torque produced by dc field winding. As L_f remains constant in the whole electrical period, the cogging torque can be neglected.

C. Conduction Model

According to the principle of six-phase DC-VRM, the conventional six states conduction is adopted, and the current chopping control is applied as the current regulator. As illustrated in (3), the conduction phases of the DC-VRM are determined by the mutual inductance between the field winding and armature windings, which can be found in Fig. 2. The positive and negative direction currents flow during the rising stage and falling stage of the mutual inductance between the field winding and armature windings, respectively. This trapezoidal inductance feature can effectively avoid the direct current jump from positive to negative and reduce the torque ripples during commutation.

D. Self-Inductance Characteristics

In the self-inductance model of six-phase DC-VRM, as shown in Fig. 3, the amplitudes of each phase are equal, and the phase differences between the adjacent phases are 60°. 0° is defined as the position where the self-inductance of phase A starts to rise. Based on the conduction mode, one electrical period can be divided into six sectors through inductance intersections. Three inductance intersections exist at the sector junction. In these intersections, the intersections composed of vertical-axis inductance curves, differed by 180°, are defined as main intersections, and the other two intersections are defined as assist intersections. Also, two middle intersections are in the middle of the sector range.

For the inductance detection-based position estimation, the inductance amplitudes near the intersections are very close, which makes it difficult to guarantee the sector estimation accuracy by comparing inductance amplitudes. So, a boundary sector exits at the sector junction, which may lead to a poor sector estimation accuracy. The boundary sector ranges produced by the assist intersection and the main intersection are shown in Fig. 4(a) and (b), respectively. A smaller boundary can be acquired by the main intersection-based sector division. That is because the slops of the inductance curves around the main intersections are obvious, thereby the changes in inductance amplitudes are easily detected, leading to a smaller boundary sector. On the contrary, around assist intersections, the slops of the inductance curves are not obvious and correspond to a larger boundary sector. So, the inductances detected around the main intersection point are more reliable compared with the assist intersection. In sensorless drive, sector estimation can first rely on the main intersections because of a smaller boundary sector. Once the detected information is wrong or missed at the main intersections, the assist intersections can be introduced to provide fault-tolerant ability.

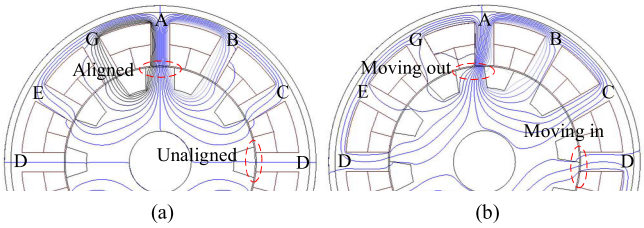

Fig. 5. Flux distributions. (a) Position α. (b) Position β.

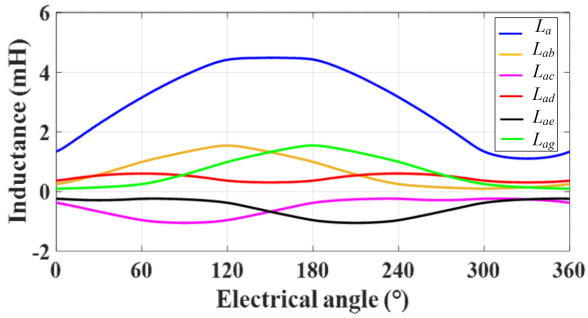

Fig. 6. Inductance curves.

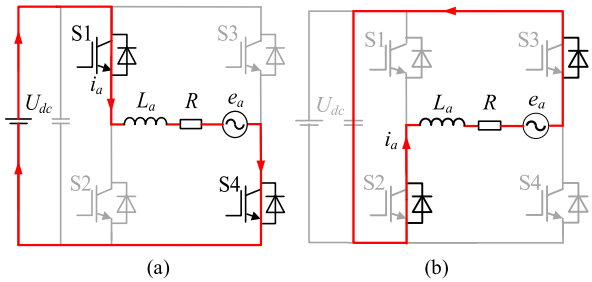

Fig. 7. Equivalent circuit. (a) Pulse injection. (b) Demagnetization.

E. Mutual-Inductance Characteristics

The finite-element analysis results of flux distributions when phase A is excited at two typical positions α and β are shown in Fig. 5(a) and (b), respectively. It is noticeable that obvious mutual coupling exits between armature windings. Among them, the mutual inductance between vertical-axis phases A and D is relatively small. That is because when phase A is in a completely aligned position, phase D is in a completely unaligned position. Meanwhile, as can be found in Fig. 5(b), the meshing trends of the rotor teeth and the stator teeth of vertical-axis phases are opposite. Therefore, the magnetic resistance between the vertical-axis phases is large, and the mutual-inductance coupling is slight. The mutual inductance can be found in Fig. 6. The fluctuation of L_{ad} is small in the whole electrical period.

III. Full-Phase APIM

A. Pulse Injection-Based Inductance Detection

Fig. 7(a) shows the equivalent circuit during pulse injection in phase A. A short detection voltage pulse is injected by switching on power transistors $S1$ and $S4$. i_a increases sharply during this stage. When the detection pulse injection is finished, the peak point value of i_a is recorded as I_a. Meanwhile, $S1$ and $S4$ are switched OFF to enter the demagnetization process, which is shown in Fig. 7(b). In this process, i_a decreases to 0.

From Fig. 7(a), the equivalent voltage equation for phase A under pulse injection can be described as

$$U_{\rm dc} = L_a \frac{di_a}{dt} + i_a \frac{dL_a}{d\theta}\omega + i_a R \tag{4}$$

where ω is the rotor angular velocity. In the initial detection and acceleration stage, ω is zero or quite small, and the back EMF can be ignored. In addition, the detection pulse duration is short, and the resultant current amplitude is small, the voltage drop on the winding can also be neglected. As the detection pulse has a short duration, it can be considered that the phase winding current rises linearly during this period. The measured self-inductance equation can be expressed as follows:

$$L_a = \frac{U_{\rm dc}\Delta t}{I_a} \tag{5}$$

where Δt is the detection pulsewidth. The sector information and the conduction phases can be decided by comparing the self-inductances. The relation can be found in Table I.

TABLE I
RELATION BETWEEN ELECTRICAL ANGLE, SELF-INDUCTANCES, CONDUCTION PHASES, AND ROTOR SECTOR

θ (°)	Inductance relation	Conduction phases	Sector
0-60	L_d>L_a&&L_b>L_e	A, D, B, E	I
60-120	L_c>L_g&&L_a>L_d	A, D, C, G	II
120-180	L_b>L_e&&L_g>L_c	B, E, C, G	III
180-240	L_a>L_d&&L_e>L_b	A, D, B, E	IV
240-300	L_g>L_c&&L_d>L_a	A, D, C, G	V
300-360	L_e>L_b&&L_c>L_g	B, E, C, G	VI

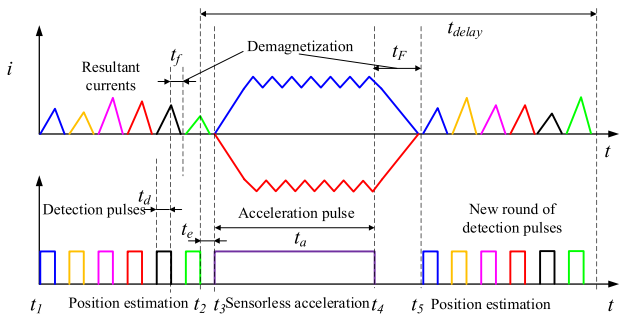

Fig. 8. Schematic diagram of full-phase APIM.

B. Full-Phase APIM

As shown in Fig. 8, to avoid the mutual-inductance influence on position estimation, the detection pulses are injected alternatively. Only one detection phase conducts at the same time; thus, the peak current sampling is not affected by mutual inductance. An operation cycle is defined as the period from t_1 to t_5 that consists of alternative detection pulses and acceleration pulses. This method is essentially a discrete sampling of the rotor position. First, the detection pulse sequence is injected from t_1 to t_2, and the resultant currents are registered. After full phases are detected, the rotor position can be estimated between t_2

and t_3. Then, the conduction phases are determined, and further acceleration pulses are injected during the period from t_3 to t_4. After each phase completes the demagnetization between t_4 and t_5, a new round of detection pulses is injected from t_5.

C. Indicators That Affect Acceleration Performance

Since full inductance intersections can be detected, when facing current sampling missing or out of reasonable range, assist intersections can be introduced for position estimation to guarantee fault-tolerant ability. While during the acceleration process, since the position information is sampled discretely, the interval of position update leads to a potential commutation delay t_{delay}, which can be expressed as

$$t_e = t_3 - t_2 \le t_{\text{delay}} \le t_5 - t_1 + t_3 - t_2 = nt_d + (n-1)t_f + 2t_e + t_a + t_F \tag{6}$$

where t_e is the estimation time, n is the number of detected phases, t_d is the width of detection pulse, t_f is the demagnetization time of detection pulse, t_a is the width of acceleration pulse, and t_F is the demagnetization time of acceleration pulse. Under a certain pulsewidth of detection pulse and acceleration pulse, t_{delay} depends on n. This kind of commutation delay will cause the lag of the commutation angle θ_{offset} or even commutation errors.

$$\theta_{\text{offset}} = \omega t_{\text{delay}}. \tag{7}$$

As θ_{offset} exits, the torque generation is constrained, thus limiting the increase of rotor speed. Furthermore, the duty cycle γ that contributes to torque generation is mainly generated by the acceleration pulses, which is defined as follows:

$$\gamma = \frac{t_5 - t_3}{t_5 - t_1} = \frac{t_a + t_F}{nt_d + (n-1)t_f + t_e + t_a + t_F}. \tag{8}$$

It is clear to see that the increase of detection time may lead to a decrease in γ, thus constraining torque production.

IV. Reduced-Phase APIM

In this six-phase DC-VRM, redundant inductance intersections exist at the sector junction. As one intersection is enough to distinguish sectors, reduced-phase APIM is a potential strategy to reduce t_{delay} and increase γ. Five-phase APIM, four-phase APIM, and three-phase APIM are the potential methods. But as n decreases, when facing the failure of current sensor sampling, reliable sector judgment is hard to be guaranteed. Meanwhile, due to the lack of main intersections, sector judgments must rely on assist intersections, thus leading to a larger boundary sector and a reduction of fault-tolerant ability. How to balance these indicators is a problem that needs to be discussed.

A. Five-Phase APIM

When the sampling of any phase is missing or wrong, the remained inductance intersections can still make the sector estimation. This character confirms the fault-tolerant ability of full-phase APIM. The schematic diagram of potential reduced-phase APIM is shown in Fig. 9.

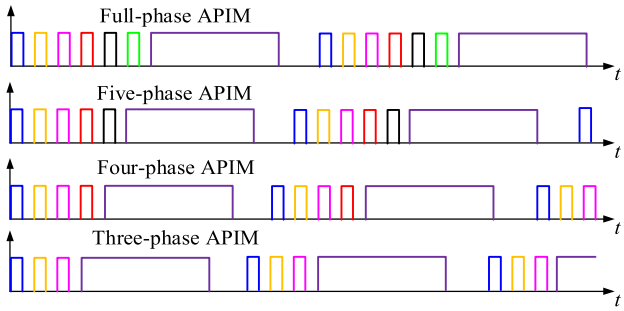

Fig. 9. Schematic diagram of reduced-phase APIM.

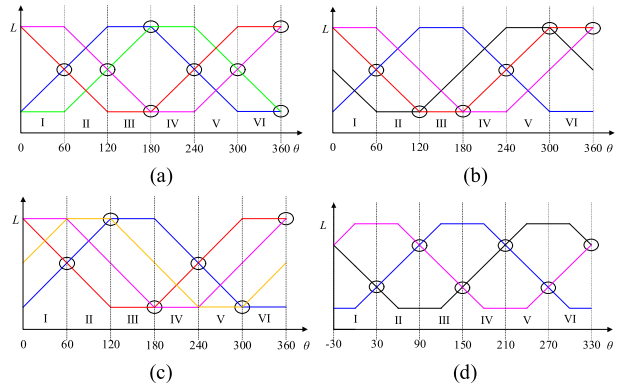

Fig. 10. Reduced-phase APIM. (a) Four-phase case 1. (b) Four-phase case 2. (c) Four-phase case 3. (d) Three-phase.

B. Four-Phase APIM

As shown in Fig. 10(a), four-phase APIM can be designed in which the lacks of two phases are on the vertical axis, thereby four main intersections remain. Otherwise, as shown in Fig. 10(b) and (c), only two main intersections remain; accordingly, more assist intersections should be introduced for position estimation.

C. Three-Phase APIM

For three-phase APIM, the interval of phases should be one-third electrical angle period to achieve a balance sector division. For example, phases A, C, and E with 120° intervals are designed as the detection phases to inject the detection pulses, while the other phase B, D, and G only inject acceleration pulses. As shown in Fig. 10(d), it is noticeable that this sector division is accompanied by a commutation offset of 30°. That is because all the intersections in this situation are middle intersections. As the existing communication offset, the torque generation is constrained. If n is less than 3, the inductances will be insufficient to make a sector judgment with necessary sector division accuracy by inductance comparison. The reduced-phase APIMs are compared in Table II. n_{main} is the number of main intersections, n_{assist} is the number of assist intersections, and n_{mid} is the number of middle intersections.

Reduced-phase APIM has an obvious effect on reducing t_{delay} and increasing γ, thus improving acceleration performance. It also proves the fault-tolerant ability when facing the current

TABLE II
COMPARISON OF REDUCED-PHASE APIM

n	n_{main}	n_{assist}	n_{mid}	t_{delay}	γ	Fault-tolerant
5	4	8	8	Large	Small	Strong
4 (case 1)	4	2	4	Middle	Middle	Middle
4 (case 2)	2	4	4	Middle	Middle	Middle
4 (case 3)	2	4	4	Middle	Middle	Middle
3	0	0	6	Small	Large	Weak

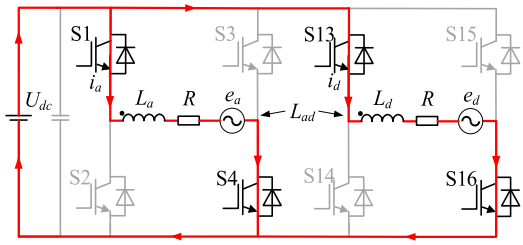

Fig. 11. Equivalent circuit of vertical-axis SPIM.

sampling fault. While with the decreasing of detected phases, the absence of inductance intersections may deprive the fault-tolerant ability and detection accuracy. Considering the above reduced-phase APIMs comprehensively, four-phase APIM case 1 shows a balance performance.

V. VERTICAL-AXIS SPIM

In this chapter, a novel vertical-axis SPIM is proposed in which the detection pulses are injected into vertical-axis phases simultaneously to halve the detection time. It can be proved that the mutual-inductance influence on the position estimation at the main intersection can be ignored. And the inductance sampling bias caused by APIM can be avoided fundamentally at the main intersection. This method not only has the merit of high fault-tolerant ability but also improves both detection accuracy and acceleration performance at the same time.

A. Vertical-Axis SPIM

The design principle of vertical-axis SPIM can be illustrated as the main intersections are composed of vertical-axis phases, and the mutual-inductance coupling between them is slight. In addition, the detected inductances of vertical-axis phases are sampled simultaneously, so no detection phase bias exists at the main intersections, which fundamentally avoids the detection error caused by APIM. The equivalent circuit and the schematic diagram of the proposed method are shown in Figs. 11 and 12, respectively.

In the period of three detection pulses, six-phase inductance information can be indirectly acquired. t_{delay} and γ can be optimized as (9) and (10), respectively

$$t_{\text{delay}} = 3t_d + 2t_f + t_e + t_a + t_F \tag{9}$$

$$\gamma = \frac{t_a + t_F}{3t_d + 2t_f + t_e + t_a + t_F}. \tag{10}$$

Fig. 13 shows the flowchart of vertical-axis SPIM. At the initial stage, vertical-axis synchronous pulses are injected, and

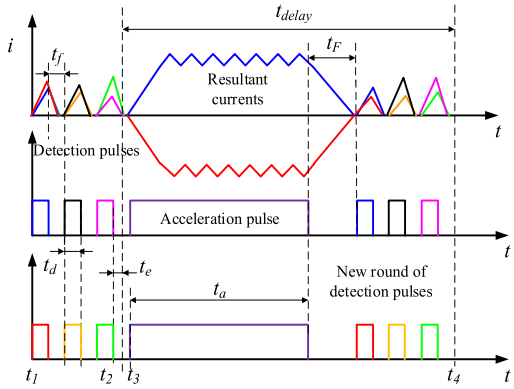

Fig. 12. Schematic diagram of vertical-axis SPIM.

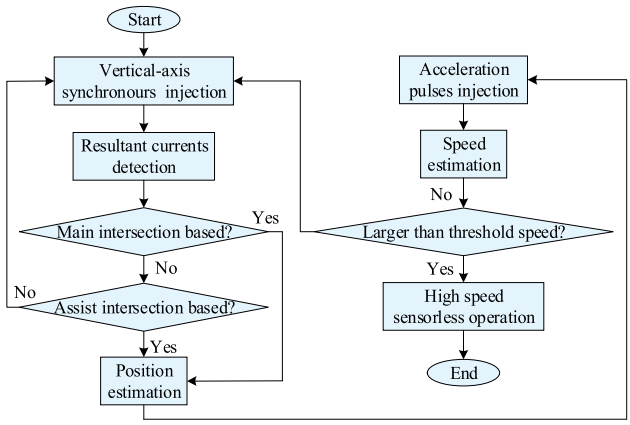

Fig. 13. Flowchart of vertical-axis SPIM.

the resultant currents are collected for comparison at the main intersection first. Once the sampled current is missing or out of reasonable range, assist intersection is introduced for position estimation. Then, the acceleration pulses are injected to drive the machine.

As position-sensorless control methods are feasible for a specific speed region, once the rotor speed is larger than the threshold speed, the control mode should be switched to high-speed sensorless drive [15], [16], [27]. To ensure a smooth transition, two methods are chosen for their effectiveness in their respective speed ranges. The transition between the two sensorless methods occurs at a threshold speed where both methods work satisfactorily [31].

To achieve a smooth full-speed sensorless drive, the threshold should be selected at a certain level. Therefore, the detected signal, such as back EMF, is large enough to be detected, thus guaranteeing the signal-to-noise ratio. To achieve more smooth transmission, the threshold speed selection often requires offline tuning by the trial-and-error methods [15], [31].

B. Analysis of Mutual-Inductance Influence

As analyzed above, the mutual-inductance coupling degree between vertical-axis phases is slight, and the range of fluctuations in the entire electrical angle period is small. When the

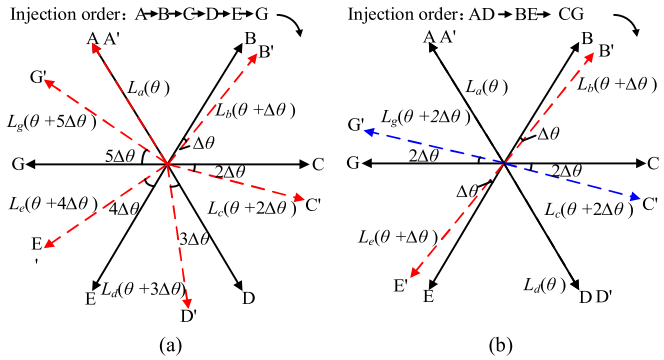

Fig. 14. Inductance vectors and sampling bias. (a) APIM. (b) Vertical-axis SPIM.

detection pulses are injected into the vertical-axis phases A and D simultaneously, the equivalent circuit equation of phases A and D are shown in (11) and (12), respectively

$$U_{\rm dc} = i_a\, R + L_a \frac{di_a}{dt} + i_a \frac{dL_a}{d\theta}\omega + L_{ad}\frac{di_d}{dt} + i_d \frac{dL_{ad}}{d\theta}\omega \tag{11}$$

$$U_{\rm dc} = i_d\, R + L_d \frac{di_d}{dt} + i_d \frac{dL_d}{d\theta}\omega + L_{ad}\frac{di_a}{dt} + i_a \frac{dL_{ad}}{d\theta}\omega. \tag{12}$$

Insert (12) into (11), the formula can be simplified as

$$(L_a - L_{ad})\frac{di_a}{dt} = (L_d - L_{ad})\frac{di_d}{dt} \tag{13}$$

$$\frac{L_d - L_{ad}}{L_a - L_{ad}} = \frac{I_a}{I_d}. \tag{14}$$

From the above analysis, due to the existence of mutual inductance, comparing I_a and I_d is comparing the magnitude relationship between L_a–L_{ad} and L_d–L_{ad} actually, which is equivalent to comparing L_a and L_d. By comparing the peak currents, the sector information can be deduced. Although the mutual inductance exists during the detection stage, this influence can be ignored.

C. Analysis of Inductance Sampling Bias

A potential factor that affects sector estimation is inductance sampling bias caused by APIM. With the rotor rotation during the acceleration stage, the sampled phase inductance inevitably has a certain phase bias, rather than being sampled simultaneously. Therefore, sector estimation error may occur, especially in the boundary sector. In APIM, the ideal inductance vectors of A, B, C, D, E, and G and the detected inductance vectors of A′, B′, C′, D′, E′, and G′ are compared in Fig. 14(a). The phase bias between two adjacent phases vectors can be described as

$$\Delta\theta = \omega(t_d + t_f). \tag{15}$$

As the interval of detection phases increases, the detection phase bias will increase accordingly. Moreover, as ω increases, the phase bias of detected inductance will increase accordingly. APIM is essentially to avoid the mutual-inductance influence on self-inductance amplitudes detection, but these methods cause the phase bias in the inductance sampling in the acceleration stage. The inherent phase deviation of detected inductance can be avoided by vertical-axis SPIM fundamentally. As shown in Fig. 14(b), the three pairs of vertical-axis phases AD, BE, and CG that compose the main intersections are detected without sample delay, thereby the accuracy of main intersection-base sector estimation can be guaranteed.

By the proposed method, full phases are detected within a half detection time. As a result, $t_{\rm delay}$ is decreased and γ is improved. It has been proved that the mutual-inductance influence on position estimation can be ignored, and no inductance sampling bias exists around the main intersections.

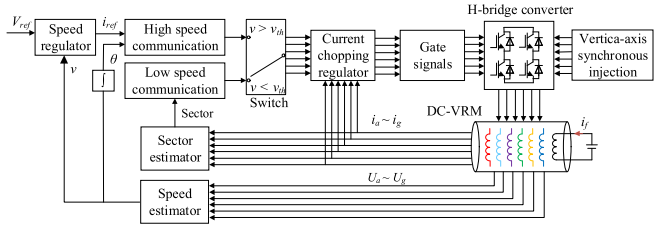

Fig. 15. Full-speed control diagram.

D. Full-Speed Sensorless Operation

Fig. 15 shows the full-speed sensorless control diagram. The resultant currents of vertical-axis detection pulses are collected for comparison through the sector estimator. In low-speed operation, the acceleration commands are generated as reference current excitation that contributes to torque generation. In this way, rotor speed can increase steadily. The current chopping regulator is applied to the current loop. Gate signals are sent to H-bridge converters directly. Once the speed reaches a certain level, the system can be switched to high-speed sensorless drive mode.

VI. Pulse Injection Closed Coil Faults Diagnosis

In this research, six-phase DC-VRM is a kind of multiphase fault-tolerant machine, and its fault-tolerant capability is improved from parallel drive topology and sensorless drive method. On the one hand, the parallel drive topology allows each phase to be driven independently, so it has the inherent fault-tolerant ability when faced with an open-circuit fault. The faulty phase will not affect the healthy phase, which effectively reduces the impact of the open-circuit fault on the overall drive performance of the machine.

On the other hand, the redundant inductance intersections can provide the fault-tolerant ability of position estimation in the absence of current detection. Both full-phase APIM and vertical-axis SPIM can sample the whole phase currents, which means a fault-tolerant threshold is provided when facing the current sampling fault. Reduce APIM can be seen as a counter-evidence method that sacrifices a part of the fault-tolerant ability to enhance acceleration performance.

For both open-circuit fault and current sensor damage, it is a common phenomenon that there is no current sensor signal in a

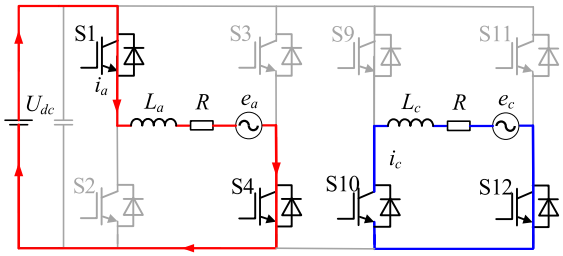

Fig. 16. Equivalent circuit of pulse injection closed coil fault diagnosis.

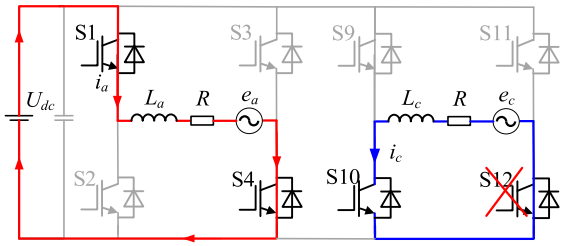

Fig. 17. Equivalent circuit of the pulse injection transistor fault diagnosis.

faulty phase. How to distinguish these two faults is investigated, and a pulse injection closed coil fault diagnosis method by armature winding mutual inductance during the initial position detection stage is proposed. In this method, a closed coil is formed in a healthy phase by switching on related power transistors to detect the induced current excited by the faulty phase. As mutual-inductance coupling exists between the armature windings, if the fault is caused by the damage of the current sensor, an induced current will be generated in the closed coil when a detection pulse is injected into the faulty phase. On the contrary, if the faulty phase suffers from an open-circuit fault, no current can be detected in the healthy phase closed coil.

The equivalent circuit of pulse injection closed coil fault diagnosis is shown in Fig. 16. For example, phase A suffers from a current sensor broken fault, and phase C is a healthy phase. By switching on transistors *S*10 and *S*12, a closed coil of phase C can be acquired, and a bidirectional induced current can pass through phase C to troubleshoot the open-circuit fault in phase A.

In addition, this method can also be used to locate the damaged transistor in an open-circuit faulty phase. In Fig. 17, phase A is a healthy phase, and phase C is an open-circuit faulty phase but with a working current sensor. By injecting a detection pulse in phase A, if the negative current can be detected, the fault can be determined as the damage of the transistor 12. Therefore, the damaged transistor can be located, and the current sensor fault can be eliminated. Through this method, fault types can be distinguished exactly, and fault-tolerant operation methods for the two fault types are introduced.

VII. Experimental Results

In this chapter, full-phase APIM, reduced-phase APIM (four-phase APIM case 1), and vertical-axis SPIM are selected for further experimental analysis.

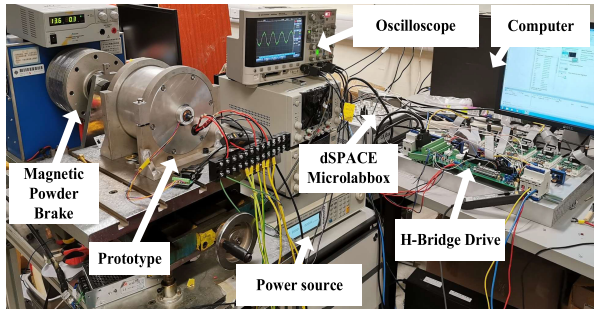

Fig. 18. Experimental setup.

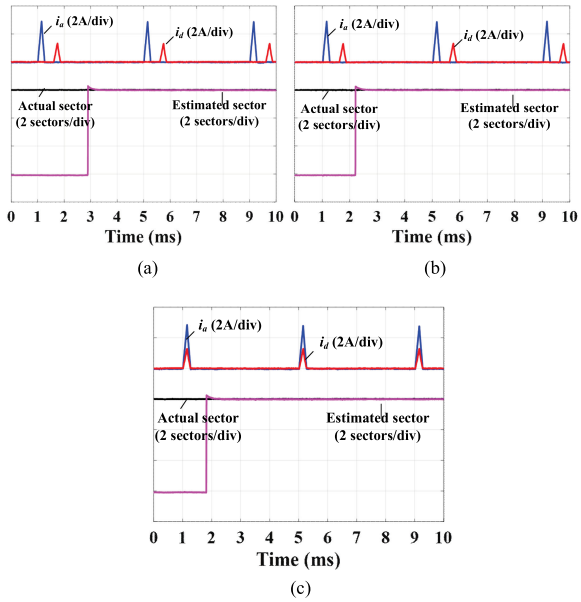

Fig. 19. Experiments of initial position detection. (a) Full-phase APIM. (b) Reduced-phase APIM. (c) Vertical-axis SPIM.

A. Experimental Setup

Experiments are carried out to verify the validity of the proposed pulse injection sensorless drive method. As the experimental setup is shown in Fig. 18, the sensorless control is performed based on a real-time control platform of a dSPACE MicroLabBox with a simulation step size of 50 μs. Control parameters can be monitored by a personal computer or oscilloscope. Commercial H-bridge converters are applied to drive the DC-VRM. The field winding is excited by the dc power source to establish the excitation magnetic field. A coaxial magnetic powder brake is connected to the DC-VRM. The actual rotor position is acquired by a resolver for reference.

B. Initial Position Detection

To acquire the initial position of the DC-VRM, detection pulses are injected into the armature windings, and then the resultant currents are compared to estimate the initial sector. The experiments of initial sector detection when the rotor is located in Sector VI are shown in Fig. 19. All the pulse injection methods can estimate the initial sector precisely, thus guaranteeing that the machine starts smoothly without reverse rotation.

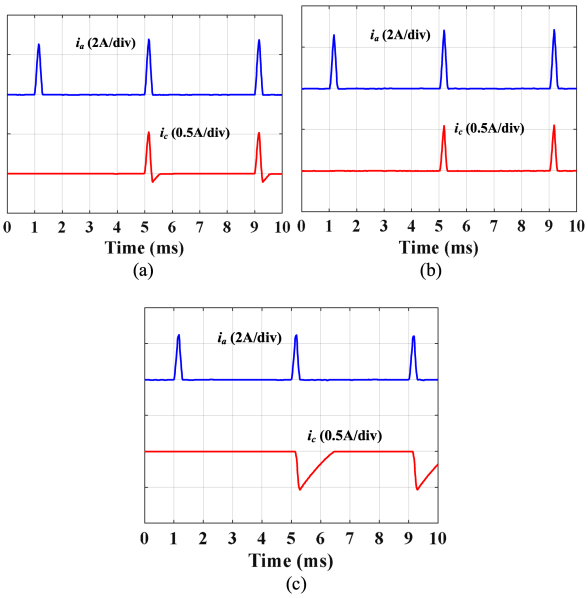

Fig. 20. Experiments of pulse injection closed coil fault diagnosis. (a) Current sensor fault. (b) Power transistor $S10$ fault. (c) Power transistor $S12$ fault.

C. Pulse Injection Closed Coil Faults Diagnosis

In the initial position detection stage, when the current sensor fails to detect the current, the proposed pulse injection closed coil faults diagnosis method can be applied. As shown in Fig. 19(a), by switching on power transistors $S10$ and $S12$, a closed coil is formed in the healthy phase C. Once the faulty phase A suffers from current sensor error without open-circuit fault, an induced current is excited in the formed closed coil. Therefore, the open-circuit fault can be excluded in phase A. Experimental results to locate a damaged power transistor in an open faulty circuit but with a working current sensor is shown in Fig. 20(b) and (c). The closed coil is formed by switching on power transistors $S10$ and $S12$. By injecting detection pulse in healthy phase A, if only one-directional current can be detected, the damaged power transistor can be located. The results are shown in Fig. 20(b) and (c), indicating that the damaged power transistor are $S10$ and $S12$, respectively.

D. Sensorless Drive Acceleration

To further compare the impact of different pulse injection methods on acceleration performance, experiments are carried out. t_d and t_a are designed as 0.15 ms and 1.25 ms, respectively. t_f and t_F are reserved as 0.2 ms and 1 ms, respectively. t_e is decided by the sampling rate of the controller, which is 0.1 ms. Load torque is 1 N·m provided by the magnetic powder brake. These parameters are kept all the same in the experiments but only with different injection methods. As can be found in Fig. 21, all these methods can achieve sensorless startup but with quite different acceleration performances. Within 1 s of acceleration time, the full-phase APIM detection method can reach the speed of 100 r/min, while the reduced-phase APIM can reach the speed of 170 r/min, both are lower than 220 r/min acquired by the vertical-axis SPIM. The proposed vertical-axis SPIM can acquire a higher acceleration and a wider acceleration range in 1 s.

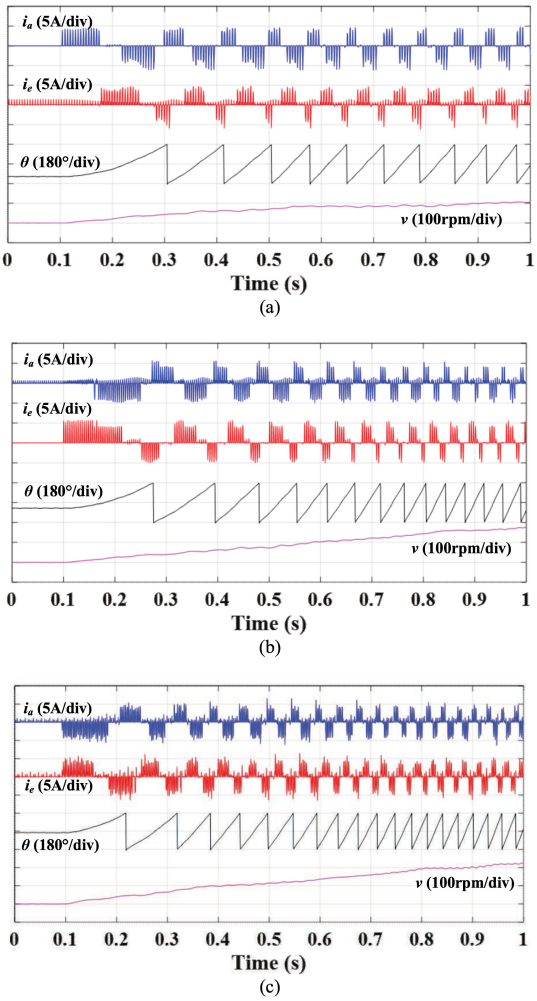

Fig. 21. Experimental results of acceleration. (a) Full-phase APIM. (b) Reduced-phase APIM. (c) Vertical-axis SPIM.

TABLE III
COMPARISON OF PULSE INJECTION METHODS

Detection methods	t_{delay}	γ	Fault-tolerant	Speed at 1s
Full-phase APIM	<4.35ms	51.7%	Strong	100rpm
Reduced-phase APIM	<3.65ms	61.6%	Weak	170rpm
Vertical-axis SPIM	<3.3ms	68.2%	Strong	220rpm

The performances of these three methods are compared in Table III. The proposed novel vertical-axis SPIM has both the merits of high acceleration performance and strong fault-tolerant ability.

VIII. DISCUSSION

In this study, pulse injection methods are optimized by minimizing the mutual-inductance coupling between phases. The mutual inductance is mainly determined by the pole pair combinations, which also can be minimized by machine design. For example, the flux linkage is closed by a short magnetic circuit in 12/10 DC-VRM. Therefore, the flux passes through the adjacent phases, thus causing mutual-inductance coupling between the armature windings. Although for 12/8 DC-VRM, the flux linkage passes through its negative phase, thereby the

mutual inductance between the adjacent phases can be ignored. The discussion of this phenomenon can be found in [8]. Also, for DC-VRM, more pole pair combinations can be applied. As discussed in [9], for 12 slots design, 12/8 and 12/14 pole pair combinations have avoidable mutual inductance between armature windings. However, the torque ripple and cogging torque of these pole pair combinations are severe. Therefore, the design of the 12/10 pole pair combination is a better choice. And the mutual-inductance influence can be minimized by the proposed vertical-axis SPIM.

It should be noticed that the proposed method is suitable for initial position estimation and acceleration. To achieve a full-speed sensorless drive and guarantee smooth transmission, the threshold speed selection requires offline tuning by the trial-and-error methods [15], [31]; more solid verifications will be conducted by combining novel high-speed sensorless drive methods in future research.

Some cost-saving drive topology can also be applied to DC-VRM sensorless drives. But their fault-tolerant ability is reduced compared with that of the H-bridge converters. In this study, we focus on the research to achieve a solution to have a strong fault-tolerant ability for the potential aerospace applications. Therefore, a parallel H-bridge converter is a better solution. A specific analysis of cost-saving topology will be carried out in a future study.

IX. Conclusion

This article proposes a novel vertical-axis SPIM for six-phase DC-VRM to improve acceleration performance and guarantee fault-tolerant ability at the same time. First, the inductance characteristics as well as their influence on sensorless control are analyzed. Then, the advantage of the multiphase machine in the sensorless drive is investigated as inductance intersections based sector division in which a smaller boundary sector can be acquired by main intersections, and fault-tolerant ability can be provided by assist intersections. Furthermore, full-phase APIM is introduced to avoid mutual inductance on position estimation, and reduced-phase APIM is discussed in terms of acceleration performance and fault-tolerant ability. Finally, vertical-axis SPIM is proposed, and it has been proved that the mutual-inductance influence on position estimation can be ignored, thereby high detection reliability and acceleration performance can be acquired without deterioration of fault-tolerant ability. The experimental results show that the proposed method has a high acceleration performance, and it can provide the fault-tolerant ability for both current sampling fault and open-circuit fault. Consequently, a solution that combines sensorless merits, low torque ripple, and fault-tolerant ability can be achieved, which has good potential to be applied as an aerostarter and generator.

References

[1] J. Cao and A. Emadi, "A new battery/ultracapacitor hybrid energy storage system for electric, hybrid, and plug-in hybrid electric vehicles," *IEEE Trans. Power Electron.*, vol. 27, no. 1, pp. 122–132, Jan. 2012.

[2] K. T. Chau, C. C. Chan, and C. Liu, "Overview of permanent-magnet brushless drives for electric and hybrid electric vehicles," *IEEE Trans. Ind. Electron.*, vol. 55, no. 6, pp. 2246–2257, Jun. 2008.

[3] I. Boldea, L. N. Tutelea, L. Parsa, and D. Dorrell, "Automotive electric propulsion systems with reduced or no permanent magnets: An overview," *IEEE Trans. Ind. Electron.*, vol. 61, no. 10, pp. 5696–5711, Oct. 2014.

[4] X. Zhao, S. Niu, X. Zhang, and W. Fu, "Design of a new relieving-DC-saturation hybrid reluctance machine for fault-tolerant in-wheel direct drive," *IEEE Trans. Ind. Electron.*, vol. 67, no. 11, pp. 9571–9581, Nov. 2020.

[5] J. Ye, B. Bilgin, and A. Emadi, "An extended-speed low-ripple torque control of switched reluctance motor drives," *IEEE Trans. Power Electron.*, vol. 30, no. 3, pp. 1457–1470, Mar. 2015.

[6] Z. Chen, H. Wang, and Y. Yan, "A doubly salient starter/generator with two-section twisted-rotor structure for potential future aerospace application," *IEEE Trans. Ind. Electron.*, vol. 59, no. 9, pp. 3588–3595, Sep. 2012.

[7] L. R. Huang, J. H. Feng, S. Y. Guo, J. X. Shi, W. Q. Chu, and Z. Q. Zhu, "Analysis of torque production in variable flux reluctance machines," *IEEE Trans. Energy Convers.*, vol. 32, no. 4, pp. 1297–1308, Dec. 2017.

[8] S. Jia, R. Qu, J. Li, D. Li, and H. Lu, "Design considerations of stator DC-winding excited vernier reluctance machines based on the magnetic gear effect," *IEEE Trans. Ind. Appl.*, vol. 53, no. 2, pp. 1028–1037, Mar./Apr. 2017.

[9] X. Liu and Z. Q. Zhu, "Stator/rotor pole combinations and winding configurations of variable flux reluctance machines," *IEEE Trans. Ind. Appl.*, vol. 50, no. 6, pp. 3675–3684, Nov./Dec. 2014.

[10] X. Zhao and S. Niu, "Design and optimization of a novel slot-PM-assisted variable flux reluctance generator for hybrid electric vehicles," *IEEE Trans. Energy Convers.*, vol. 33, no. 4, pp. 2102–2111, Dec. 2018.

[11] T. Dos Santos Moraes, N. K. Nguyen, E. Semail, F. Meinguet, and M. Guerin, "Dual-multiphase motor drives for fault-tolerant applications: Power electronic structures and control strategies," *IEEE Trans. Power Electron.*, vol. 33, no. 1, pp. 572–580, Jan. 2018.

[12] I. Gonzalez-Prieto, M. J. Duran, F. Barrero, M. Bermudez, and H. Guzmán, "Impact of postfault flux adaptation on six-phase induction motor drives with parallel converters," *IEEE Trans. Power Electron.*, vol. 32, no. 1, pp. 515–528, Jan. 2017.

[13] F. Genduso, R. Miceli, C. Rando, and G. R. Galluzzo, "Back EMF sensorless-control algorithm for high-dynamic performance PMSM," *IEEE Trans. Ind. Electron.*, vol. 57, no. 6, pp. 2092–2100, Jun. 2010.

[14] G. Wang, M. Valla, and J. Solsona, "Position sensorless permanent magnet synchronous machine drives—A review," *IEEE Trans. Ind. Electron.*, vol. 67, no. 7, pp. 5830–5842, Jul. 2020.

[15] E. Ofori, T. Husain, Y. Sozer, and I. Husain, "A pulse-injection-based sensorless position estimation method for a switched reluctance machine over a wide speed range," *IEEE Trans. Ind. Appl.*, vol. 51, no. 5, pp. 3867–3876, Sep./Oct. 2015.

[16] D. Xiao, J. Ye, G. Fang, Z. Xia, X. Wang, and A. Emadi, "Improved feature-position-based sensorless control scheme for SRM drives based on nonlinear state observer at medium and high speeds," *IEEE Trans. Power Electron.*, vol. 36, no. 5, pp. 5711–5723, May 2021.

[17] M. Ehsani, I. Husain, and A. B. Kulkarni, "Elimination of discrete position sensor and current sensor in switched reluctance motor drives," *IEEE Trans. Ind. Appl.*, vol. 28, no. 1, pp. 128–135, Jan./Feb. 1992.

[18] M. Ehsani, I. Husain, S. Mahajan, and K. R. Ramani, "New modulation encoding techniques for indirect rotor position sensing in switched reluctance motors," *IEEE Trans. Ind. Appl.*, vol. 30, no. 1, pp. 85–91, Jan./Feb. 1994.

[19] J. Cai, Z. Liu, Y. Zeng, H. Jia, and Z. Deng, "A hybrid-harmonic-filter-based position estimation method for an SRM with embedded inductive sensing coils," *IEEE Trans. Power Electron.*, vol. 33, no. 12, pp. 10602–10610, Dec. 2018.

[20] S. M. Ahmed and P. W. Lefley, "A new simplified sensorless control method for a single phase SR motor using HF signal injection," in *Proc. 42nd Int. Univ. Power Eng. Conf.*, 2007, pp. 1075–1078.

[21] J. Ye, B. Bilgin, and A. Emadi, "Elimination of mutual flux effect on rotor position estimation of switched reluctance motor drives," *IEEE Trans. Power Electron.*, vol. 30, no. 3, pp. 1499–1512, Mar. 2015.

[22] J. Cai and Z. Liu, "An unsaturated inductance reconstruction based universal sensorless starting control scheme for SRM drives," *IEEE Trans. Ind. Electron.*, vol. 67, no. 11, pp. 9083–9092, Nov. 2020.

[23] H. Gao, F. R. Salmasi, and M. Ehsani, "Inductance model-based sensorless control of the switched reluctance motor drive at low speed," *IEEE Trans. Power Electron.*, vol. 19, no. 6, pp. 1568–1573,Nov. 2004.

[24] M. Krishnamurthy, C. S. Edrington, and B. Fahimi, "Prediction of rotor position at standstill and rotating shaft conditions in switched reluctance machines," *IEEE Trans. Power Electron.*, vol. 21, no. 1, pp. 225–233, Jan. 2006.

[25] G. Pasquesoone, R. Mikail, and I. Husain, "Position estimation at starting and lower speed in three-phase switched reluctance machines using pulse injection and two thresholds," *IEEE Trans. Ind. Appl.*, vol. 47, no. 4, pp. 1724–1731, Jul./Aug. 2011.
[26] J. Cai and Z. Deng, "Sensorless control of switched reluctance motor based on phase inductance vectors," *IEEE Trans. Power Electron.*, vol. 27, no. 7, pp. 3410–3423, Jul. 2012.
[27] Y. Zhao, H. Wang, H. Zhang, and L. Xiao, "Position-sensorless control of DC + AC stator fed doubly salient electromagnetic motor covered full speed range," *IEEE Trans. Ind. Electron.*, vol. 62, no. 12, pp. 7412–7423, Dec. 2015.
[28] X. Zhou and B. Zhou, "Rotor position estimating scheme for doubly salient EM machine sensorless startup," *Electron. Lett.*, vol. 53, no. 15, pp. 1033–1034, Jul. 2017.
[29] X. Zhou, B. Zhou, and J. Wei, "A novel position-sensorless startup method for DSEM," *IEEE Trans. Ind. Appl.*, vol. 54, no. 6, pp. 6101–6109, Nov./Dec. 2018.
[30] X. Zhou, B. Zhou, K. Wang, L. Zhang, and Y. Zhao, "Two-step rotor position estimation method for doubly salient electromagnetic starter-generator over zero and low speeds range," *IEEE J. Emerg. Sel. Topics Power Electron.*, vol. 9, no. 3, pp. 2664–2673, Jun. 2021.
[31] A. Khalil *et al.*, "Four-quadrant pulse injection and sliding-mode-observer-based sensorless operation of a switched reluctance machine over entire speed range including zero speed," *IEEE Trans. Ind. Appl.*, vol. 43, no. 3, pp. 714–723, May/Jun. 2007.

Weiyu Wang (Graduate Student Member, IEEE) is currently working toward the Ph.D. degree in electrical engineering with the Department of Electrical Engineering, Hong Kong Polytechnic University, Hong Kong.

His research interests include electrical machine drive and position-sensorless drive.

Xing Zhao (Member, IEEE) received the B.Eng. degree from the Nanjing University of Aeronautics and Astronautics, Nanjing, China, in 2014, and the Ph.D. degree from The Hong Kong Polytechnic University, Hong Kong, in 2020, both in electrical engineering.

From July 2019 to January 2020, he was a Visiting Research Scholar with the Center for Advanced Power Systems, Florida State University, Tallahassee, FL, USA. Between July 2020 and October 2021, he served as a Research Assistant Professor with the Department of Electrical Engineering, The Hong Kong Polytechnic University. Since November 2021, he has been a Lecturer with the Department of Electronic Engineering, University of York, York, U.K. He has authored or coauthored more than 50 technical papers in the international journals and conferences and holds six granted patents. His research interests include advanced electrical machines, motor drives, and power electronics for electric vehicles and renewable energy systems.

Shuangxia Niu (Senior Member, IEEE) received the B.Sc. and M.Sc. degrees from the School of Electrical Engineering and Automation, Tianjin University, Tianjin, China, in 2002 and 2005, respectively, and the Ph.D. degree from the Department of Electrical and Electronic Engineering, The University of Hong Kong, Hong Kong, in 2009, all in electrical engineering.

Since 2009, she has been with The Hong Kong Polytechnic University, Hong Kong, where she is currently an Associate Professor with the Department of Electrical Engineering. She has authored or coauthored more than 100 articles in leading journals. Her research interests include novel electrical machines and drives, renewable energy conversion systems, and applied electromagnetics.

Weinong Fu received the Ph.D. degree from The Hong Kong Polytechnic University (PolyU), Hong Kong, in 1999.

He is a Professor with the Shenzhen Institutes of Advanced Technology, Chinese Academy of Sciences, Shenzhen, China. He worked with PolyU about 13 years as an Associate Professor and a Full Professor. He was one of the key developers with Ansoft Corporation, Pittsburgh, USA. He has about seven years of working experience with Ansoft, focusing on the development of commercial software Maxwell, which is a leading commercial software package for the computation of electromagnetic fields of electromechanical equipment. During 1982–1986, he worked with Shanghai Electrical Apparatus Research Institute, where he accumulated valuable experience to deal with the design and manufacturing of electric devices in practice and constructed a solid foundation for further academic career development. He has made many contributions to the theory and application of electromagnetic field computation and electric device design, including the publication of more than 250 refereed journal papers. He regularly serves as a paper reviewer for IEEE TRANSACTIONS ON MAGNETICS, IEEE TRANSACTIONS ON ENERGY CONVERSION, IEEE TRANSACTIONS ON INDUSTRIAL ELECTRONICS, IEEE TRANSACTIONS ON POWER ELECTRONICS, IEEE TRANSACTIONS ON INDUSTRY APPLICATIONS, *Energies,* and *COMPUMAG*, *CEFC*, and *INTERMAG* international conferences. His research interests mainly focus on computational electromagnetics, optimal design of electric devices, applied electromagnetics, and novel electric machines.